Materials for life sciences

From phytomedicine to photomedicine: quercetin-derived carbon nanodots—synthesis, characterization and healthcare applications

Gaurav Gopal Naik[1,4] ⓘ, Ravi Pratap[2] ⓘ, Debadatta Mohapatra[1] ⓘ, Singh Shreya[1] ⓘ, Deepak K. Sharma[1] ⓘ, Avanish S. Parmar[2] ⓘ, Arjun Patra[3] ⓘ, and Alakh N Sahu[1,*] ⓘ

[1] *Department of Pharmaceutical Engineering & Technology, IIT (BHU), Varanasi 221005, India*

[2] *Department of Physics, IIT (BHU), Varanasi 221005, India*

[3] *Department of Pharmacy, Guru Ghasidas University, Bilaspur 495551, India*

[4] *Department of Pharmaceutical Chemistry, Yashwantrao Bhonsale College of Pharmacy, Affiliated to Mumbai University, Sawantwadi 416510, India*

ABSTRACT

In this report, we present the hydrothermal method-driven synthesis of carbon nanodots (CNDs) using quercetin and further evaluate the effects of surface passivation on their physicochemical and biological attributes. The quercetin-derived CNDs (qCD) were surface passivated with polyethylene glycol to produce qCD-Pg. Firstly, the qCD was employed as a fluorescent nanoprobe that can selectively sense arsenic (As^{3+}) with a limit of detection (LOD) of 0.598 μM through enhancement in fluorescence emission. It was revealed that upon surface fabrication with polyethylene glycol, qCD lost its ability to sense As^{3+}, but qCD-Pg selectively detected iron (Fe^{3+}) with a LOD of 0.324 μM. The developed method was validated as per International Conference on Harmonization Harmonised Tripartite Guideline (ICH Topic Q 2 (R1). The applicability of the qCD and qCD-Pg-based sensing method for the quantification of As^{3+} and Fe^{3+} in a real sample (tap water) was also analyzed. Further, the qCD-Pg was conjugated with andrographolide (Ad) to produce qCD-Pg-Ad and explored as a nanocarrier for its delivery. These conjugates prolonged and improved the drug release, leading to an enhanced cytotoxic effect on leukemia cancer cells (K-562). Also, the qCD-Pg-Ad complex had a better anticancer effect on K-562 than free form and showed very low cytotoxicity to normal kidney cells (Vero), indicating specific anticancer activity to the leukemia. These CNDs considerably inhibited the growth of multidrug resistant bacterial strains and exhibited significant free radical scavenging potential. These nanodots showed good thermal stability, colloidal dispersion stability, and photostability. Overall, the findings of our study demonstrated
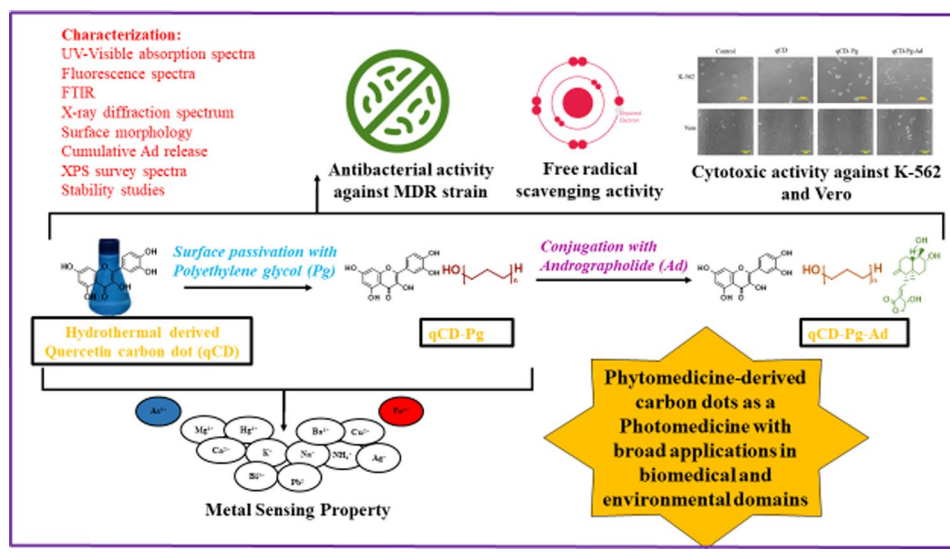
 Springer

phytomedicine-derived CNDs as photomedicine with broad applications in biomedical and environmental domains.

GRAPHICAL ABSTRACT

Introduction

Nanoprobes are integrated systems over 100 times smaller than cells, with sizes smaller than pores and apertures in the human body's vasculature and tissues. They integrate fundamental concepts from chemical biology and material science to investigate and design novel nanomaterials [1, 2]. Because nanoprobes can easily incorporate valuable compounds such as active targeting moieties, imaging agents, or medicines through conjugation or simple loading, they offer wide applications across biomedical and environmental domains [3, 4]. Smart design and innovative development can impart multi-functional attributes to nanoprobes. CNDs have been widely exploited in recent times to develop smart nanoprobes [5]. Carbon nanotubes, nanowires, plasmonic nanoparticles, and magnetic nanoparticles are some of the other nanoprobes that are among the most common [6]. CNDs can be easily fabricated using various cost-effective and environment-friendly methods, and biomolecules can be used to achieve the requisite biosensing properties. They have been reported to possess applications in bioimaging, drug delivery, metal sensing, antibacterial agents, etc. [7, 8].

Flavonoids are ubiquitous polyphenolic chemicals characterized by the flavan nucleus and are found in a wide range of fruits, vegetables, and plant-derived beverages. Quercetin is a polyphenolic compound bearing a flavone moiety with two benzene rings linked by a heterocyclic pyrrole ring and diphenyl propane basic skeleton. It exhibits anticancer, anti-inflammatory, and antioxidant potential in various studies reported in cellular and animal models via regulating gene expression and signaling pathways [9].

Water contamination owing to heavy metals such as arsenic, lead, mercury, etc., affects human life to a greater extent. To date, traditional sophisticated analytical techniques, such as atomic fluorescence spectrometry (AFS), atomic absorption spectroscopy (AAS), inductively coupled plasma-mass spectrometry (ICP-MS), mass spectroscopy (MS), inductive coupled mass atomic emission spectrometry (ICP-AES), ion-exchange chromatography, and plasmon resonance Rayleigh scattering (PRRS) spectroscopy, are widely used for quantification of such metal ions [10, 11]. However, conventional detection methods are expensive and tedious to use. Hence, it is essential to explore other alternatives for the timely and economical detection of heavy metals.

PEGylation of protein/peptide therapeutics and conventional nanoparticles is frequently employed using polyethylene glycol, since it is a non-immunogenic and highly water-soluble polymer.

Polyethylene glycol has recently been widely investigated for its unique capacity to enhance carbon nanodot fluorescence emission [12]. Ad is the major phytomolecule in *Andrographis paniculata* (AP), belonging to the family of Acanthaceae, which has been projected as a potential medicinal moiety in various traditional medicinal systems. Biological activities such as anticancer, anti-inflammatory, and antioxidant have been reported for this diterpenoid lactone [13]. The sustained release of therapeutics into the tumor microenvironment is acquiring much attention due to high efficacy, low systemic side effects, and prolonged therapeutic activity. Ad was chosen as a model drug to evaluate the capacity of synthesized CNDs as a drug carrier. We hypothesize that upon conjugation with qCDs-Pg, the cytotoxic effect of andrographolide will be improved due to the synergistic effect, and the therapeutic outcomes will be observed for a prolonged period due to the sustained release profile of the conjugate.

To the best of our knowledge, this is the first original report demonstrating the utility of quercetin-based carbon nanodots as a fluorescent nanoprobe for As^{3+} and Fe^{3+} sensing, drug delivery, anticancer therapy, antimicrobial therapy, and free radical scavenger.

Materials and methods

All procured solvents and reagents were of analytical grade and used directly without further purification. Quercetin (#Q4951) and sulforhodamine B (#S9012) were procured from Sigma-Aldrich. 1, 1-diphenyl-2-picrylhydrazyl (DPPH) (#D9132), methanol (#34,860), dichloromethane (#34,586), etc., were purchased from Merck. Deionized water was obtained using a Millipore water purification system.

Cell lines and cell culture

Leukemia cancer (K-562) cells and normal Vero cell lines were procured from National Centre for Cell Sciences (NCCS), Pune, India, and were maintained in a humidified 5% CO_2 chamber (Thermo Hepa class 100) under optimal conditions (37 °C). Each cell line was handled carefully, passaged, and plated in culture plates, as per the need for desired experiments.

Authentication of plant specimen by DNA fingerprinting and isolation of andrographolide

The leaves of AP were collected from the Indian Institute of Technology (BHU), Varanasi campus, and used for isolation of Ad for its use as a model drug. The collected leaves were authenticated using DNA fingerprinting with the *matK* gene. The DNA was isolated as per the previous method with slight modifications [14]. The detailed experimental protocol is described in supplementary file (Sect. 1). Briefly, DNA was isolated using NucleoSpin® Plant II Kit (Macherey–Nagel). The isolated DNA was stored at 4 °C. Agarose gel electrophoresis was carried out for quality check of isolated DNA. The electrophoresis was performed with 0.5X Tris–Borate-EDTA (TBE) at 75 V. The gels were visualized in a UV transilluminator (Genei), and the image was captured under UV light using a gel documentation system (Bio-Rad). The DNA amplification was carried out in a polymerase chain reaction (PCR) thermal cycler (GeneAmp PCR System 9700, Applied Biosystems) using *MATK*-XF (Forward) and *MATK* –NR1 (Reverse) primers. The PCR products were checked by agarose gel electrophoresis and visualized in a UV transilluminator. The removal of unwanted primers and deoxynucleoside triphosphates (dNTPs) from a PCR product mixture was carried out by ExoSAP-IT (GE Healthcare). The sequencing reaction was done in a PCR thermal cycler (GeneAmp PCR System 9700, Applied Biosystems) using the BigDye Terminator v3.1 Cycle sequencing Kit (Applied Biosystems, USA) following the manufacture's protocol. The sequence quality was checked using sequence scanner software v1 (Applied Biosystems). Sequence alignment and required editing of the obtained sequences were carried out using Geneious Pro v5.1. The detailed protocol for the isolation of the Ad is described in supplementary file (Sect. 1.2).

Synthesis of CNDs, loading of andrographolide and their characterization

A simple, one-step hydrothermal synthesis approach was employed to synthesize quercetin-derived CNDs. Following earlier literature, the loading and release behavior of the qCD-Pg-Ad complex was investigated [15, 16]. The CNDs and their conjugated form were characterized using various techniques (UV spectroscopy, Fourier-transform infrared spectroscopy (FTIR),

proton nuclear magnetic resonance (^{1}H NMR), and carbon nuclear magnetic resonance (^{13}C NMR)). The detailed procedure is provided in the supplementary file (Sect. 2).

Characterization

The absorption behavior of the synthesized CNDs was investigated using a UV–vis spectrophotometer (Cary 60 UV vis, Agilent, USA). The fluorescence attributes of CNDs were studied by employing a Fluorolog-Horiba fluorescence spectrophotometer (HORIBA, France). Fourier transform infrared spectrometer (Nicolet iS5, Thermo Fisher Scientific, USA) examined the surface functional groups in 4000–400 cm^{-1}. A high-resolution transmission electron microscopy (HRTEM) (Tecnai G2 20 TWIN, FEI, USA) was used to study their morphology, and the average particle size was computed after measuring the size of 50 particles with ImageJ software (NIH, Bethesda, Maryland). Elemental analysis was performed using energy-dispersive X-ray spectroscopy (EDAX Inc.'s TEAM EDS SYSTEM), and selected area diffraction (SAED) patterns were obtained from the additional feature of the HRTEM instrument. The X-ray photoelectron spectroscopy (XPS) was carried out using XPS instrument (K-Alpha, Thermo Fisher Scientific, USA). Rigaku Miniflex 600 Desktop X-ray Diffraction System (Rigaku Corporation, Tokyo, Japan) was utilized to obtain X-ray diffraction (XRD) patterns of nanodots. Apart from this, colloidal dispersion stability (by measuring zeta potential), photostability (UV illumination with an excitation wavelength of 350 nm), and thermal stability (using TGA-50 thermogravimetric analyzer, Shimadzu, Japan) of CNDs were also investigated.

Healthcare applications

CNDs as a metal sensing probe

The sensing ability of various metal ions by qCD and qCD-Pg was studied as per earlier reported studies with slight modifications [11]. The sensing selectivity toward various metal cations such as Mg^{2+}, Hg^{2+}, Fe^{3+}, Ba^{2+}, Cu^{2+}, Ca^{2+}, K^+, Na^+, NH_4^+, As^{3+}, Ag^+, Bi^{3+}, and Pb^{2+} was investigated. Further, the sensitivity study was carried out by incubating the CNDs with sensed metal ions at various concentrations and evaluating the change in the fluorescence intensity. Detailed experimental protocol for metal sensing has been provided in supplementary file (Sect. 3).

Validation of the analytical method

The developed method was validated as per International Conference on Harmonization Harmonised Tripartite Guideline (ICH Topic Q 2 (R1), Step 4 version, Validation Of Analytical Procedures: Text And Methodology) for linearity, range, accuracy (% recovery), precision (repeatability and intermediate precision: intra-day and inter-day, inter-lab variation, and inter-personnel variation), limit of detection (LOD), and limit of quantification (LOQ) [17].

Analysis of As^{3+} and Fe^{3+} in real sample The applicability of the qCD and qCD-Pg-based sensing method for the quantification of As^{3+} and Fe^{3+} in a real sample (tap water) was studied using the earlier methods with certain modifications [11].

Cytotoxic potential of CNDs against K-562 Leukemia cell lines

The cytotoxicity potential of the CNDs and their conjugates was evaluated against K-562 Leukemia cancer cells and normal Vero cell lines at different concentrations. The cytotoxicity was investigated by sulforhodamine B (SRB) colorimetric assay, and the growth inhibition (GI_{50}) (µg/mL) was calculated using previously described methods [18]. The detailed procedure is provided in the supplementary file (Sect. 4).

Antibacterial potential of CNDs

The antibacterial activities of qCD, qCD-Pg, and qCD-Pg-Ad were evaluated using the previously reported disk diffusion method with slight modifications [19]. The antibacterial activity was evaluated against clinically isolated multi-drug resistant (MDR) bacterial strains: *Enterobacter cloacae* [20], *Escherichia coli* [21], *Klebsiella pneumonia* [22], *Enterococcus faecium* [23], and *Staphylococcus aureus* [24]. The detailed experimental protocol is described in the supplementary file (Sect. 5).
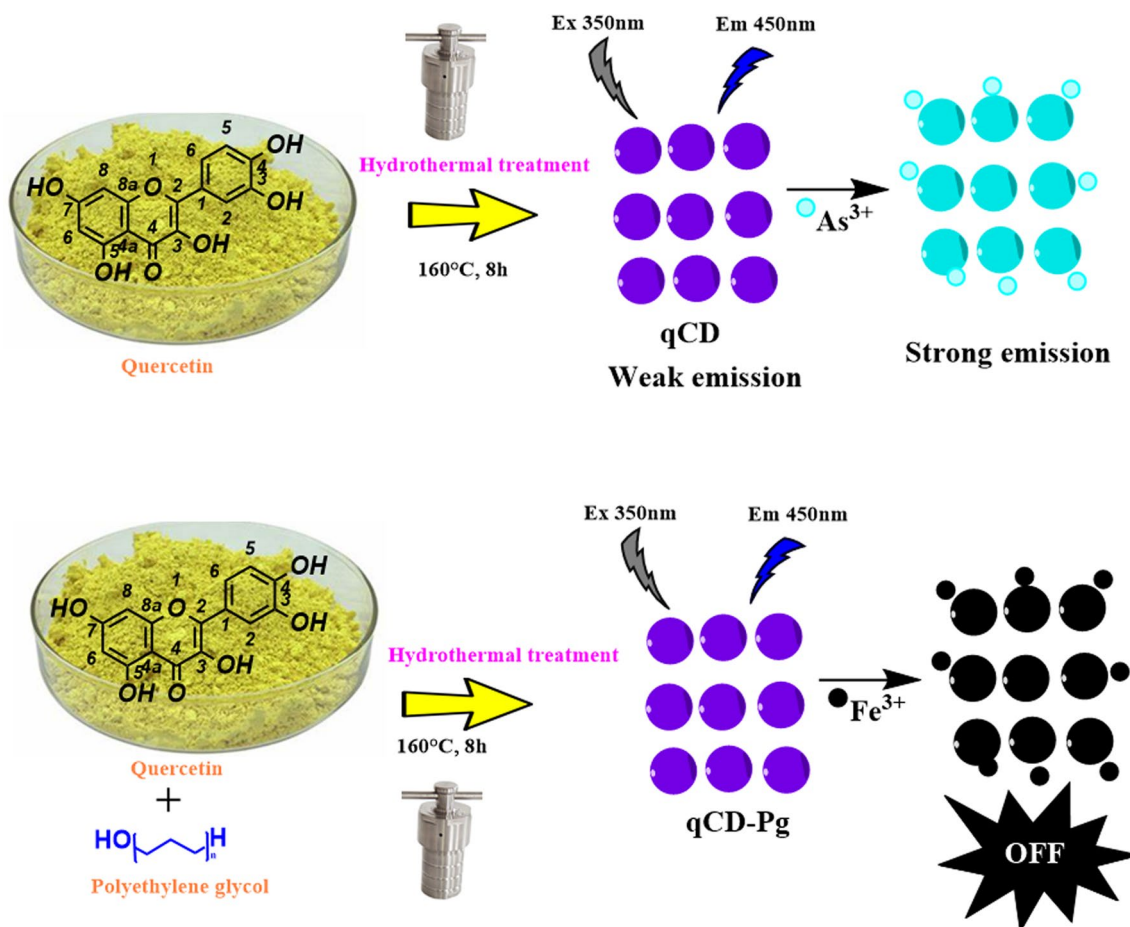
Scheme 1 Schematic representation of the synthetic process for quercetin-based carbon nanodots via a one-step hydrothermal treatment and their applications in sensing As^{3+} and Fe^{3+}.

Free Radical scavenging potential of CNDs

Free radicals scavenging potential of qCD, qCD-Pg, and qCD-Pg-Ad was evaluated according to the previously reported method with slight modifications [25]. The percent radical scavenging activity of various CNDs was calculated and compared. The detailed experimental protocol is described in the supplementary file (Sect. 6).

Statistical analysis

At least three independent experiments were performed to obtain significant data expressed as mean ± SEM. The statistical analysis was carried out using Student's t test in GraphPad Prism version 5.0.

The $P < 0.05$ was used as the criterion for statistical significance.

Results and discussion

This study focused on the quercetin-derived CNDs as a drug nanocarrier for andrographolide and as a sensing probe for As^{3+} and Fe^{3+}. Most of the earlier studies have reported the fabrication of CNDs from whole plant parts/extracts. However, in this report the CNDs have been fabricated using one of the phytoconstituent "quercetin' and explored for various healthcare and environmental applications. The quercetin-derived CNDs (qCD) were prepared successively and surface passivated with polyethylene glycol to produce qCD-Pg via a simple one-step

hydrothermal treatment at 160 °C for a period of 8 h as depicted in Scheme 1. The outcomes of DNA barcoding with the *matK* gene verified the authenticity of the AP leaves. The results of UV spectroscopy, FTIR, ^{1}H NMR, and ^{13}C NMR of isolated Ad are shown in Figure S1. Isolated Ad had a melting point of 234.9 ± 0.5 °C. The obtained data were corroborated with the reported literature data [26].

Under a UV lamp, the qCD, qCD-Pg, and qCD-Pg-Ad emitted a strong blue-green fluorescence. Figure 1a exhibits the UV–Vis absorption spectra of CNDs which revealed peaks at 255 and 367 nm, attributed to π to π^* and n to π^* transitions, respectively. Absorption peaks in the 300–400 nm range may correspond to transitions related to C=N and C=O groups. The qCD-Pg-Ad showed a slightly altered absorption pattern compared to the qCD and qCD-Pg. The typical absorption band
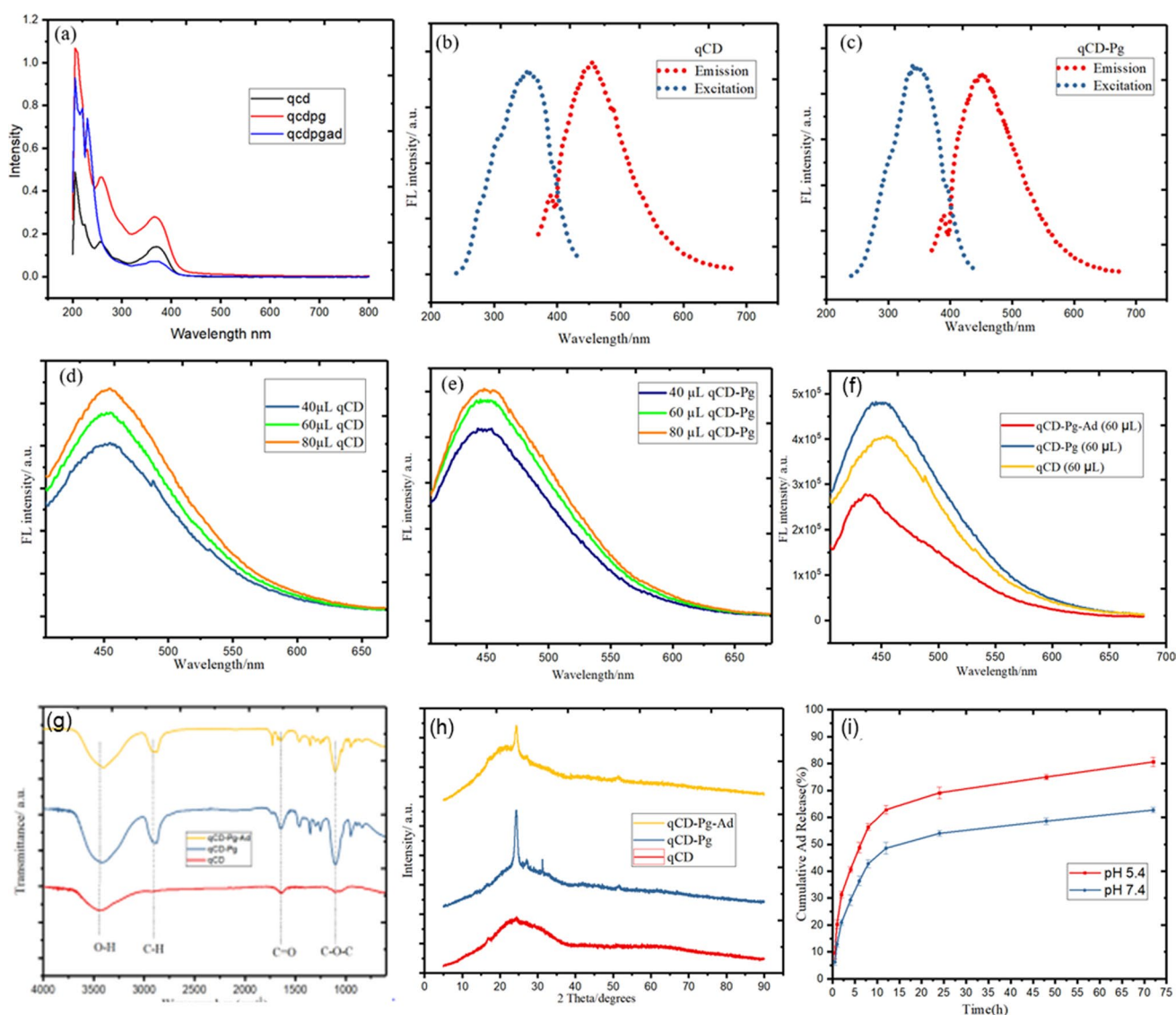

Figure 1 Optical properties, FTIR spectroscopy, XRD, and release study **a** UV–visible absorption spectra of carbon nanodots **b** Excitation and emission spectra of qCD **c** Excitation and emission spectra of qCD-Pg **d** concentration-dependent fluorescence spectra of qCD at an excitation wavelength of 350 nm **e** concentration-dependent fluorescence spectra of qCD-Pg at an excita-
tion wavelength of 350 nm, **f** comparative fluorescence spectra of qCD, qCD-Pg, qCD-Pg-Ad **g** FTIR spectrum of qCD and qCD-Pg, and qCD-Pg-Ad, **h** X-ray diffraction spectrum of qCD, qCD-Pg, and qCD-Pg-Ad, and **i** cumulative Ad release from qCD-Pg-Ad at pH 7.4 and 5.4.

of Ad at 230 nm (Fig. 1a) revealed its existence in the qCD-Pg-Ad conjugate. When excited at 350 nm, qCD and qCD-Pg showed the maximum fluorescence intensity at 450 nm (Fig. 1b and Fig. 1c). Figure 1d and e shows the concentration-dependent fluorescence spectra of qCD and qCD-Pg (mentioned volume of original CNDs diluted up to 3 mL with water). The qCD-Pg-Ad showed an altered fluorescence behavior compared to qCD and qCD-Pg. A blue shifting was observed in the case of qCD-Pg-Ad with an emission maximum of 435 nm likely demonstrating the successful conjugation of the Ad (Fig. 1f).

FTIR analysis was used to assess the presence of surface functionalities on CNDs, and the findings are displayed in Fig. 1g. The CND's OH/NH and carbonyl stretching were attributed to broad peaks at around 3936 and 1645 cm^{-1}, respectively. Peaks between 1215 and 985 cm^{-1} could be related to oxygen-containing functional groups' C–O stretching vibrations. Solubility and stability are provided by the polar functional groups that occur on the surface of CNDs. In addition to these peaks, qCD-Pg-Ad had two sharp peaks at 1723 and 1672 cm^{-1}, implying that Ad could interact with qCD-Pg via electrostatic interactions [27–29]. The XRD pattern of qCD demonstrated poor crystallinity compared to qCD-Pg and qCD-Pg-Ad Fig. 1h. The prepared carbon nanodots' XRD patterns showed a strong peak at $2\theta = 24.3°$ ($d = 0.36$ nm) and a small peak at $2\theta = 27.06°$ ($d = 0.33$ nm) corresponding to the diffractions at amorphous carbon phase and graphitic carbon, respectively [30, 31]. The average % drug loading efficiency (DLE) of the qCD-Pg-Ad was found to be 29.3 ± 0.4%. The results of Ad release at 5.4 and pH 7.4 are shown in Fig. 1i. As depicted in Figure S2, the free Ad showed rapid release behavior with more than 70% release at 2 h. The free drug (unconjugated Ad) exists independently and does not possess any interaction with the qCDs-Pg; hence, the only thing that happens during the dialysis is the exchange of dialysis media with the internal media (inside a bag) and solubilization of free andrographolide into the bulk of media, which is a rapid process. In contrast, in the case of qCD-Pg-Ad, it showed a biphasic release pattern with an initial burst release up to 8 h followed by a sustained release pattern up to 72 h. The initial phase of drug release may be due to weak physical adsorption of the drug on CND' surfaces; however, stronger interactions between CNDs and the drug could have led to a sustained release pattern [32, 33]. Also, the biphasic pattern could possibly be due to

homomolecular interactions between drug-drug in the outer layer, leading to the fast release of the drug. In contrast, heteromolecular interaction between carbon nanodots–drug on the surface could be responsible for the sustained release of the drug. The initial burst release may assist in killing cancerous cells in a short period, and sustained drug release would maintain the required therapeutic dose [34, 35]. The Ad release rate from the conjugates was significantly higher at pH 5.4 than at pH 7.4 (Fig. 1i), demonstrating its possible use in the acidic tumor microenvironment.

The results of HRTEM (Fig. 2a and b) showed an average diameter of 1.3–1.9 nm and 3.0–3.8 nm for qCD and qCD-Pg, respectively, while qCD-Pg-Ad was 4.2–4.9 nm (Fig. 2c). The slight increase in the diameter may be attributed to the conjugation with Ad. The CNDs were found to be roughly spherical shaped and evenly distributed. The SAED patterns of CNDs revealed diffused rings, confirming their amorphous phase. The amorphous form of CNDs indicates that they were appropriately fabricated.

The EDAX results (Fig. 2d and e) showed a significant amount of oxygen, carbon, and nitrogen. Figure 3a shows the XPS spectra of qCD, which revealed three distinct peaks corresponding to C 1 s, N 1 s, and O 1 s at 285.08, 400.54, and 532.08 eV, respectively, which confirmed the availability of C, N, and O containing functional groups on the surface of CNDs. In the C 1 s spectrum of qCD, peaks at 285.9 and 284.4 eV could be attributed to C-O/C-S/C-N bonds and C–C bonds, respectively (Fig. 3b). Figure 3c shows N 1 s spectra of qCD, which revealed two peaks at 400.4 eV (C–N–C) and 401.5 eV (quaternary ammonium groups). In the O 1 s spectrum of qCD (Fig. 3d), peaks at 531.9 and 533.1 eV could correspond to C=O and COH/COC, respectively [36, 37].

Figure 3e shows the XPS spectra of qCD-Pg. In the C 1 s spectrum of qCD-Pg, peaks at 285.9 and 284.7 eV could be attributed to C–O/C–S/C–N and C–C bonds, respectively (Fig. 3f). The C=O bond was attributed to the peak at 287.8 eV. Figure 3g shows N 1 s spectra of qCD-Pg, revealing two peaks at 400.1 eV (C–N–C) and 401.3 eV (quaternary ammonium groups). In the O 1 s spectrum of qCD (Fig. 3h), peaks at 531.9 and 533.1 eV could correspond to C=O and COH/COC, respectively [36, 37]. The XPS and FTIR results confirmed the presence of various functional groups in different forms, which may be responsible for variations in their physicochemical and biological profiles.
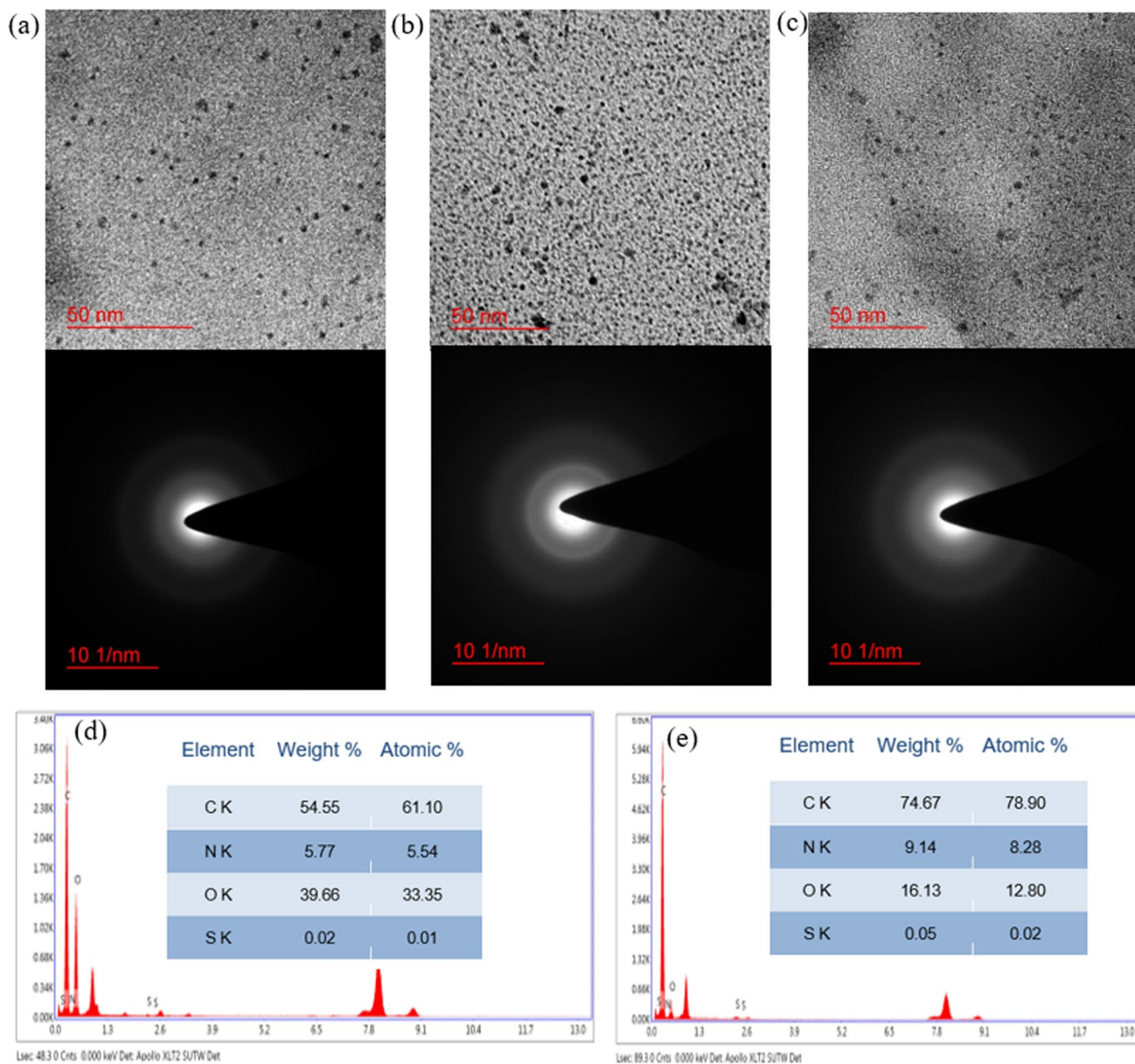
Figure 2 Surface morphology, SAED, and EDAX of carbon nanodots and its conjugates **a** HRTEM photomicrograph at 50 nm scale and SAED pattern of qCD **b** HRTEM photomicrograph at 50 nm scale and SAED of qCD-Pg **c** HRTEM photo- micrograph at 50 nm scale and SAED of qCD-Pg-Ad **d** EDAX spectra of qCD with inset data showing the elements with their corresponding percentage and **e** EDAX spectra of qCD-Pg with inset data showing the elements' corresponding percentages.

The results of zeta potential (ZP) are shown in Fig. 4 a. The ZP of qCD was −18.10 mV, whereas the ZP was drastically changed in the case of qCD-Pg and found to be −7.1 mV. The qCD-Pg-Ad complex exhibited a ZP value of −16.6 mV, demonstrating possible conjugation with Ad. The TGA thermogram shown in Fig. 4b indicates the thermal behavior of CNDs in terms of weight loss at different temperatures. A three-step degradation pattern was observed in the thermograms of qCD and qCD-Pg with very negligible weight loss up to 280 °C, reflecting their thermal stability up to this temperature. The curve leveled off after 999 °C, and a small quantity of carbon nanodots remained as burnt carbon. Earlier studies [30, 31] have made simi- lar observations. The photostability studies of qCD and qCD-Pg were studied by exposing them to UV
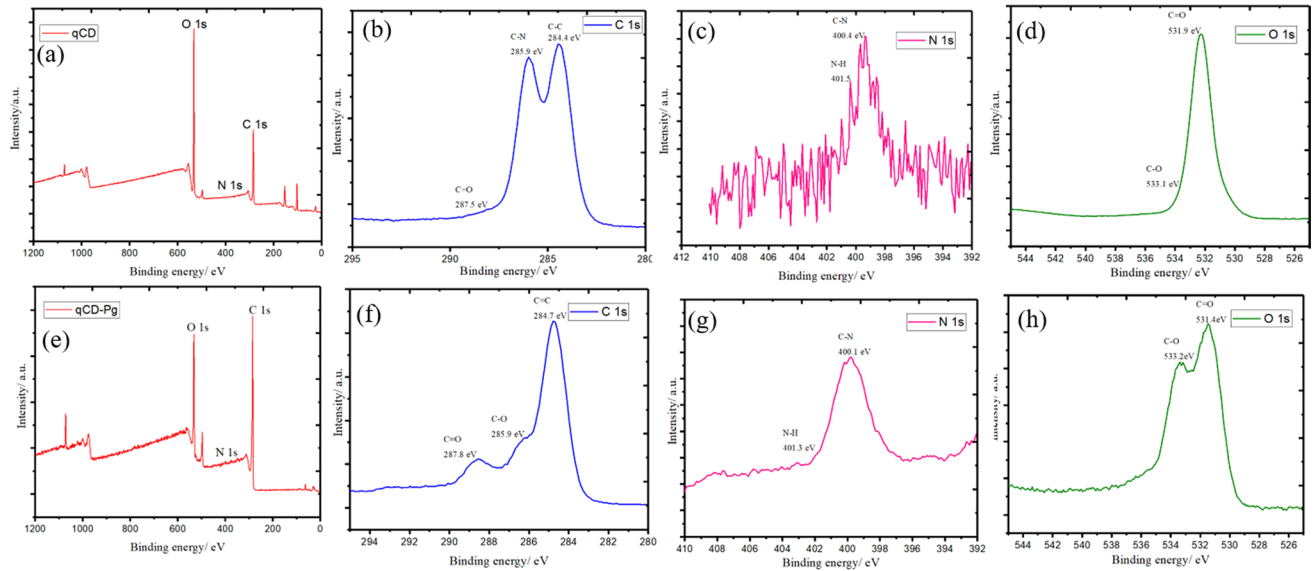
Figure 3 XPS results of CNDs **a** XPS survey spectra of the qCD, **b** XPS high-resolution survey scan of C 1 s, **c** N 1 s, and **d** O 1 s region of qCD, **e** XPS survey spectra of the qCD-Pg, **f** XPS high-resolution survey scan of C 1 s, **g** N 1 s, and **h** O 1s region of qCD-Pg.
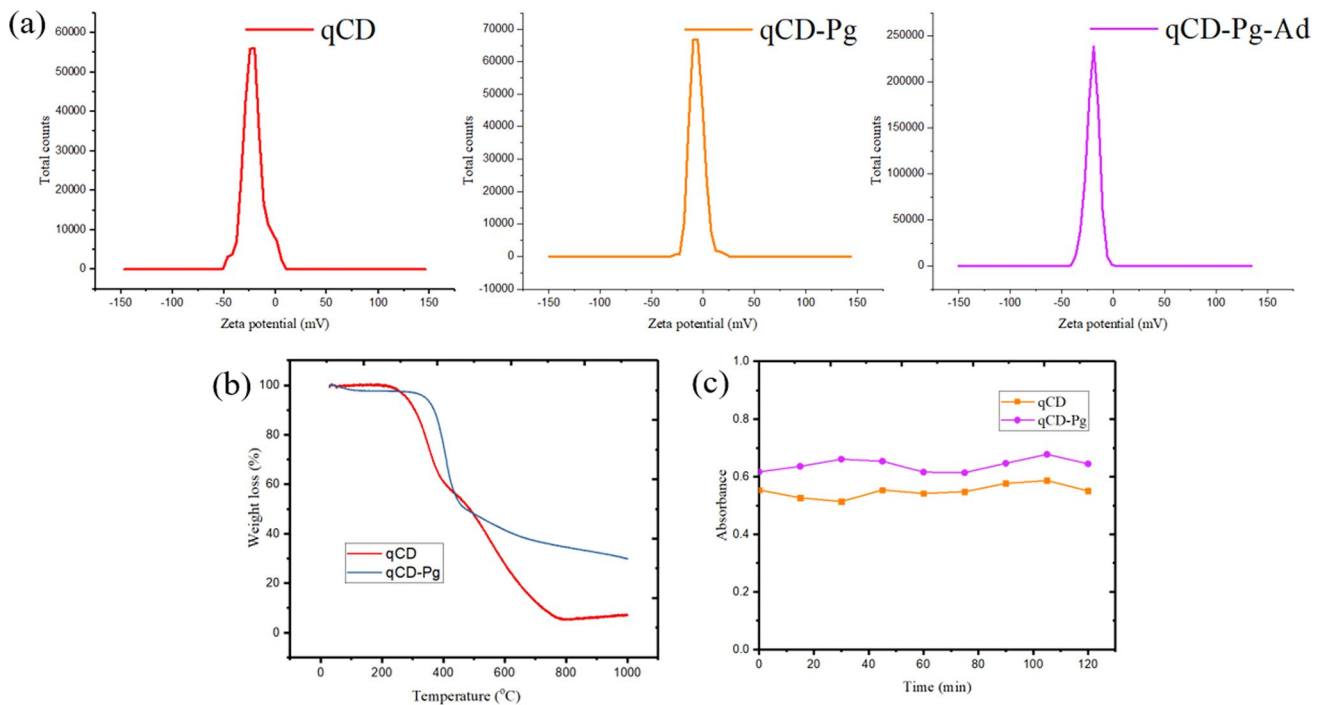

Figure 4 Stability studies of CNDs **a** ZP of qCD, qCD-Pg, qCD-Pg-Ad **b** TGA thermogram, and **c** photostability study.

light for 120 min and then determining the changes in absorbance at different time points. As shown in Fig. 4c, no significant photobleaching of carbon nanodots was observed after continuous UV exposure.

CNDs as a metal sensing probe

Water pollution has been a significant concern for the healthcare community. Due to the rapid growth of industrial pollution and lack of efficient

water-treatment technologies, it has become challenging to curb polluted water-borne ailments sufficiently. Heavy metal ions are one of the major pollutants of the environment and are a significant threat to living beings. Arsenic is one of the heavy pollutant metals which predominantly exist in various chemical forms in water bodies. The As^{3+} ions possess high solubility, mobility, and toxicity. The As^{3+} impart serious risk to some vital organs, like lungs, liver, kidneys etc. Moreover, rice, which is a staple food for most of the people, can accumulate a high concentration of As^{3+} in soil, as compared to other cereals. Considering the potential environmental risk and ecotoxicological hazard of As^{3+}, the European Union and the US Environmental Protection Agency (EPA) have listed it among the top pollutants. Hence, the accurate qualitative and quantitative analysis of As^{3+} is of utmost required for the protection of the environment and living beings [10].

Fe^{3+} is an essential ion in living beings that involves in many cellular events, such as oxygen metabolism, oxygen uptake, electronic transfer, cellular respiration, hemoglobin, and DNA synthesis. However, its deficiency and excess amount in the body lead to multiple health issues, like anemia, β-thalassemia, renal failure, tissue damage, hemochromatosis, multiple organ failures, and eventually death [38, 39]. For balanced regulation of biological events, the Fe^{3+} should be within an optimal physiological range. Hence it should be precisely analyzed in biological and environmental samples. CNDs can be successfully used for sensing heavy metals, thereby assisting in achieving United Nations' Sustainable Development Goal 6, i.e., Clean Water and Sanitation.

Selectivity is a critical criterion for evaluating a nanoprobe's performance. Thus, we investigated the differences in fluorescence emission intensity by adding various biologically and environmentally relevant metal ions (including Mg^{2+}, Hg^{2+}, Fe^{3+}, Ba^{2+}, Cu^{2+}, Ca^{2+}, K^+, Na^+, NH^{4+}, As^{3+}, Ag^+, Bi^{3+}, and Pb^{2+}) to the qCD at a concentration of 200 μM and obtaining the corresponding fluorescence emission spectra. Among the metal ions, As^{3+} demonstrated enhancement of the fluorescence intensity of qCD, whereas Fe^{3+} showed the quenching of the fluorescence intensity. Furthermore, to investigate the impact of various metal ions, on the fluorescence behavior of surface functionalized qCD-Pg, they are tested in a similar way. It was observed that qCD-Pg was unable to selectively sense As^{3+} due to a change in the nature of surface functional groups but retained the ability to sense Fe^{3+}.

As a result, a sensitivity titration was carried out at various As^{3+} concentrations ranging from 0 to 200 μM. The emission of the qCD at 450 nm progressively increased as the concentration of As^{3+} increased, as shown in Fig. 5a. The enhancement of fluorescence intensity was noticed even at low concentrations of As^{3+}, demonstrating the sensitivity of the qCD toward the sensing of As^{3+}.

The relation between F_0/F and As^{3+} concentration is presented in the inset figure (Fig. 5b). A correlation value (R^2) of 0.998 found a good linear relationship within 40–100 μM of As^{3+}. The calculated LOD was found to be 0.598 μM. In the case of qCD, adding As^{3+} results in a significant increase in fluorescence compared to the control. The aggregation process, which subsequently produced the aggregation-induced enhanced emission (AIEE) mechanism activity of qCD, is thought to be caused by the complex formation and intramolecular and extramolecular interactions. AIEE active probes are mildly emissive in the aggregate state but become substantially emissive in the aggregate state. Non-radiative decay routes are hindered in the aggregate state due to restricted intramolecular rotation. As a result, increased emission triggered by aggregation, where analytes aggregate through electrostatic, metal coordination, and hydrogen bonding, can be employed as a sensing probe. This behavior also helps to overcome flaws in traditional fluorophores, such as aggregation-triggered quenching, fluorescence bleaching, and asymmetric emission [40–42]. Multiple intermolecular contacts between qCD and arsenic ions caused aggregation, blocking non-radiative decay pathways and populating the radiative decay pathways. The presence of several functional groups on the surface of qCD, such as OH and O, may explain its adsorptive behavior, and arsenic ion species can bind to qCD via intramolecular or extramolecular interactions or adsorption [43].

Gurung et al. has reported similar results of fluorescence enhancement by As^{3+} and fluorescence quenching by Fe^{3+} addition to *Cynodon dactylon*-derived carbon quantum dots. Since the As^{3+} ions on the surface interact electrostatically with the functional groups due to its closed shell 3d-orbital (electronic configuration $= ls^2 2s^2 2p^6 3s^2 3p^6 \, 3d^{10} 4s^2$), no trap states have developed in the band gap. As^{3+} thus causes the fluorescence signal to switch on [44]. In another study, Alam et al. reported fluorescence turning on upon adding As^{3+} to chlorophyll-functionalized carbon quantum dots [45]. Alam et al. employed
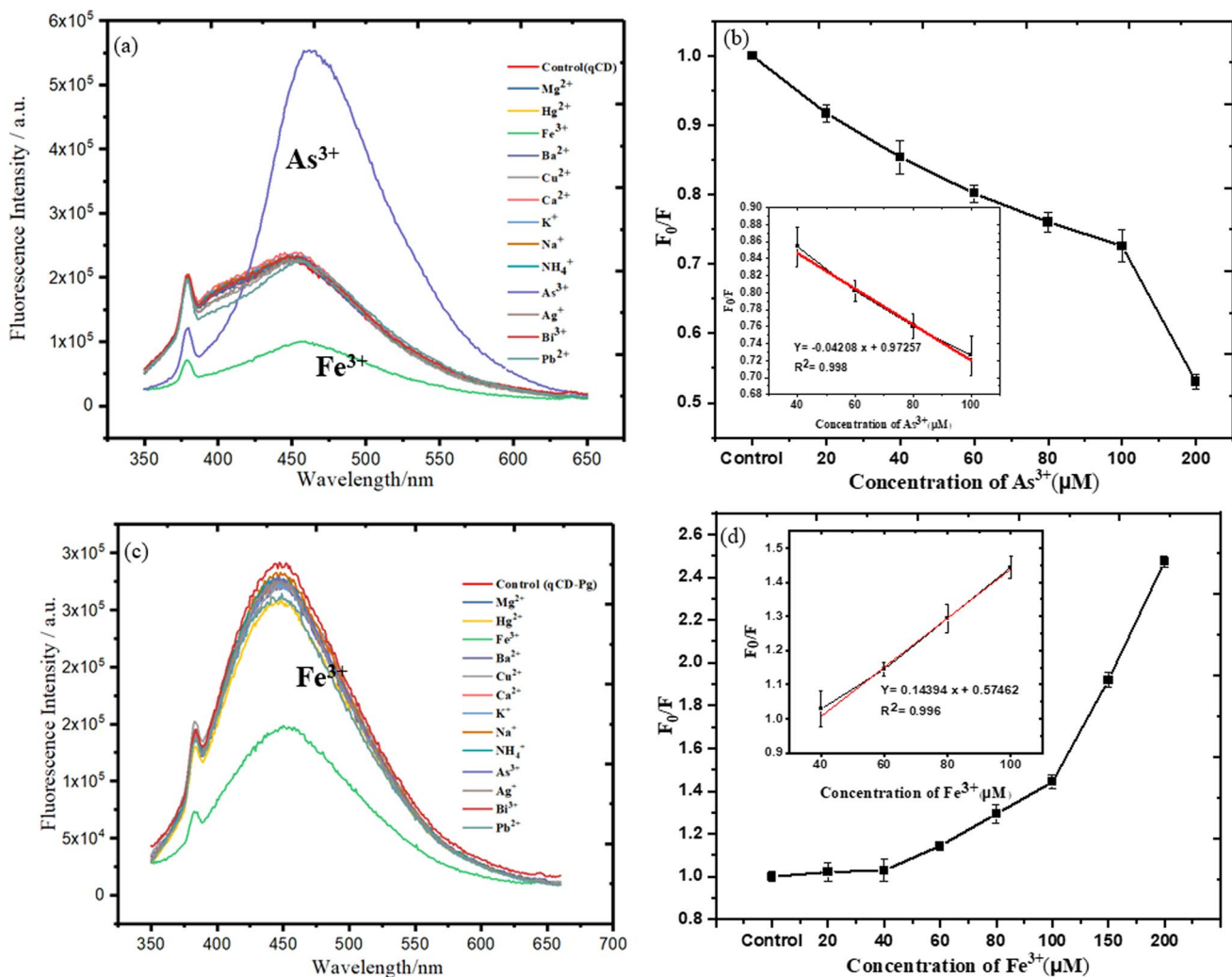
Figure 5 Sensing of metal ions using CNDs **a** Fluorescence response of qCD toward various metal ions. The control represents the fluorescence response of the carbon nanodots without any metal ions. **b** Fluorescence intensity of qCD versus concentration of As^{3+} from 0 to 200 µM (inset image showing linearity, with F_0 and F being the fluorescence intensities in the absence and presence of As^{3+}, respectively.) **c** Fluorescence responses of qCD-Pg toward various metal ions. The control represents the fluorescence response of the carbon nanodots without any ion and **d** Fluorescence intensity of qCD-Pg versus concentration of Fe^{3+} from 0 to 200 µM (inset image showing linearity, with F_0 and F being the fluorescence intensities in the absence and presence of Fe^{3+}, respectively).

surface-sensitive X-ray photoelectron spectroscopy studies to demonstrate that As^{3+} firmly binds to the carbonyl group of the CQDs' chlorophyll moiety. Furthermore, interactions of As^{3+} at the atomic level were comprehended using theoretical calculations based on Density Functional Theory (DFT).

For Fe^{3+} sensing (Fig. 5c), ground-state complex formation, collision quenching, excited-state reaction, molecule rearrangement, and energy transfer are intermolecular interactions responsible for fluorescence quenching [46, 47]. Static quenching and dynamic quenching are two types of quenching mechanisms. The electron transfers from excited qCD-Pg to half-filled 3d orbitals of Fe^{3+} caused strong non-radiative electron/hole recombination, resulting in aggregation-induced emission quenching [48], indicating that Fe^{3+} ions bind to the functional groups on the surface of qCD-Pg to form Fe^{3+} chelates. As a result of the coordination of Fe^{3+} on the surface of qCD-Pg with nitrogen-bearing groups, carboxyl and hydroxyl, the radiation transition is destroyed, and fluorescence quenching occurs [46, 48]. The interaction of several hydroxyl

and carboxyl functional groups on the surface of the carbon nanodots, as observed in the FTIR spectrum, may have caused the quenching upon coming in contact with Fe^{3+}. This non-radiative transfer of electrons between the electron-rich carbon nanodots and the electron-deficient Fe^{3+} ions has the effect of turning off the fluorescence [45, 49, 50, 51].

A sensitivity titration was also carried out at various Fe^{3+} concentrations of qCD-Pg ranging from 0 to 200 μM (Fig. 5d). The emission of the qCD-Pg at 450 nm steadily declined as the concentration of Fe^{3+} increased; this demonstrates that the current sensing system is susceptible to Fe^{3+}. The relationship between F_0/F and Fe^{3+} concentration is shown in the inset figure (Fig. 5d) shows a good linear relationship between the linear ranges at 40–100 μM, with a correlation coefficient (R^2) of 0.996. The calculated LOD was found to be 0.324 μM.

Results of validation

Linearity and range

The average F_0/F of threements against their respective concentrations of As^{3+} and Fe^{3+} is presented in Fig. 5b and d. A linear relationship was obtained between the selected concentrations of As^{3+} (40–100 μM) and the F_0/F values with correlation coefficients ($r^2 = 0.998$) and regression equation $-0.04208\,x + 0.97257$ ($n = 3$).

Similarly, a linear relationship was found between the used concentrations of Fe^{3+} (40–100 μM) and the corresponding F_0/F values with correlation coefficients ($r^2 = 0.996$) and regression equation $0.14394\,x + 0.57462$ ($n = 3$). The high correlation coefficient values ($r^2 = 0.99$) in both cases of the fitted model indicate a strong relationship among the variables.

Accuracy

The closeness of theoretical and experimental values indicates the accuracy of the analytical method. The results of the accuracy of As^{3+} and Fe^{3+} in terms of % recovery and percentage relative standard deviation (% RSD) were represented in Table S5. The high recovery values and low percent RSD (< 2%) reflect the excellent accuracy of the developed fluorescence-based metal sensing method.

Precision

Precision represents the closeness of agreement among a series of readings obtained from multiple specimens of the same homogeneous sample under specified analytical conditions. In the present study, the repeatability and intermediate precision (intra-day, inter-day, inter-lab variation, and inter-personnel variation) studies were performed to examine the precision of the fluorescence-based metal sensing method for various concentrations (40, 60, and 80 μM) of metal solution.

The % RSD values obtained from the repeatability study were found to be below 2% (Table S6). The results of intermediate precision studies were shown in Table S7. Except few results of inter-personnel variation and inter-lab variations, the % RSD values were lesser than 2%, which represents a high degree of precision of the developed fluorescence-based metal sensing method. The slight fluctuation in the results is due to the instrumental or handling errors by person.

LOD and LOQ

The LOD and LOQ values for the determination of As^{3+} were found to be 0.598 and 1.812 μM, respectively, as represented in Table 1. Similarly, the LOD and LOQ values for Fe^{3+} were found to be 0.324 and 0.9833 μM, respectively. The lower values of LOD and

Table 1 LOD and LOQ values of As^{3+} and Fe^{3+}

Analyte	Equation	Standard error of y intercept (SE)	Standard deviation of y intercept (SE/$\sqrt{N}$)	LOD (μM) (3.3×SD of y)/slope	LOQ (μM) (10×SD of y)/slope
As^{3+}	$-0.04208x + 0.97257$	0.0145	0.00725	0.598	1.812
Fe^{3+}	$0.14394x + 0.57462$	0.0283	0.01415	0.324	0.9833

LOQ of the developed fluorescence-based metal sensing method indicated the sensitivity of the optimized method for analysis of As^{3+} and Fe^{3+}.

Analysis in real sample

The addition of As^{3+} spiked water samples to the qCD resulted in an increase in the fluorescence. In contrast, the tap water (un-spiked) incubated with qCD showed no change in the fluorescent intensity due to the absence of As^{3+}. In the case of Fe^{3+} spiked water samples, the quenching of the fluorescence intensity of qCD-Pg was observed. Also, the qCD-Pg in the presence of un-spiked tap water showed slight quenching of the fluorescent intensity. The slight quenching of the fluorescent intensity might be due to the presence of little amount of iron in the tap water, which was found to be below the quantification limit. The results of % recovery and % RSD are shown in Table 2. The recovery was found to be within 98.24–99.48%, and the RSD was found to be 0.867–1.314%. Such a high recovery (> 98%) with a low RSD (< 2%) demonstrates the accuracy and analytical ability of the fluorescence-based metal sensing method for the quantitative analysis of As^{3+} and Fe^{3+} in real water samples.

Cytotoxic potential of CNDs against K-562 leukemia cell lines

Leukemia, which accounts for 28% of cases, is the most prevalent cancer in children, followed by tumors of the brain and other nerve systems (26%), roughly one-third of which are benign or malignant tumors [52]. Ad, a major diterpenoid from AP has been reported to exhibit anticancer activity against leukemia [53, 54]. We hypothesized that upon conjugation with CNDs, the cytotoxic effect of Ad would be improved due to the synergistic effect, and the therapeutic outcomes would be observed for a prolonged period due to the sustained release profile of the qCD-Pg-Ad conjugate. The results of SRB assay against K-562 leukemia and normal vero cell lines are shown in Fig. 6a and b, respectively. The GI_{50} values of Ad, qCD, qCD-Pg, and qCD-Pg-Ad were found to be 60.2, 45.5, 52.6, and 42.8 µg/mL, respectively. The GI_{50} value of Ad was found to be decreased when complexed with qCD-Pg due to the synergistic activity, indicating its possible use to treat leukemia. The standard adriamycin (ADR) showed a GI_{50} value of 10.2 µg/mL. Interestingly, no substantial cytotoxicity was seen in the normal kidney (Vero) cell line (Fig. 6b). The brightfield photomicrographs (Fig. 6c) reflected the morphological alteration with spherical morphology of K-562 leukemia cells in the presence of various treatments. In contrast, no morphological alteration was observed in the case of CNDs treated normal Vero cell line, indicating the cancer-selective cytotoxic potential of the CNDs. However, the standard ADR was found to be cytotoxic to the Vero cell line.

Antibacterial potential of CNDs

Owing to rise in incidences of bacterial resistance to conventional antibiotics, it is the need of the hour to explore potent antibacterial. In recent times, CNDs have garnered a lot of interest as a viable replacement for traditional antimicrobial agents due to their superior antibacterial potential and biocompatibility [55, 56]. In this study, the antibacterial activity of qCD, qCD-Pg and qCD-Pg-Ad was examined against different clinically isolated MDR bacterial strains, i.e., *Escherichia coli* (−), *Klebsiella pneumonia* (−), *Enterobacter cloacae* (−), *Enterococcus faecium* (+), and *Staphylococcus aureus* (+) using disk diffusion method with slight modifications. Each of CNDs (dried form) was diluted with DMSO, and 20 µL of each CNDs (1000 µg/mL)

Table 2 Quantitative estimation of As^{3+} and Fe^{3+} in tap water using qCD and qCD-Pg as fluorescent probe

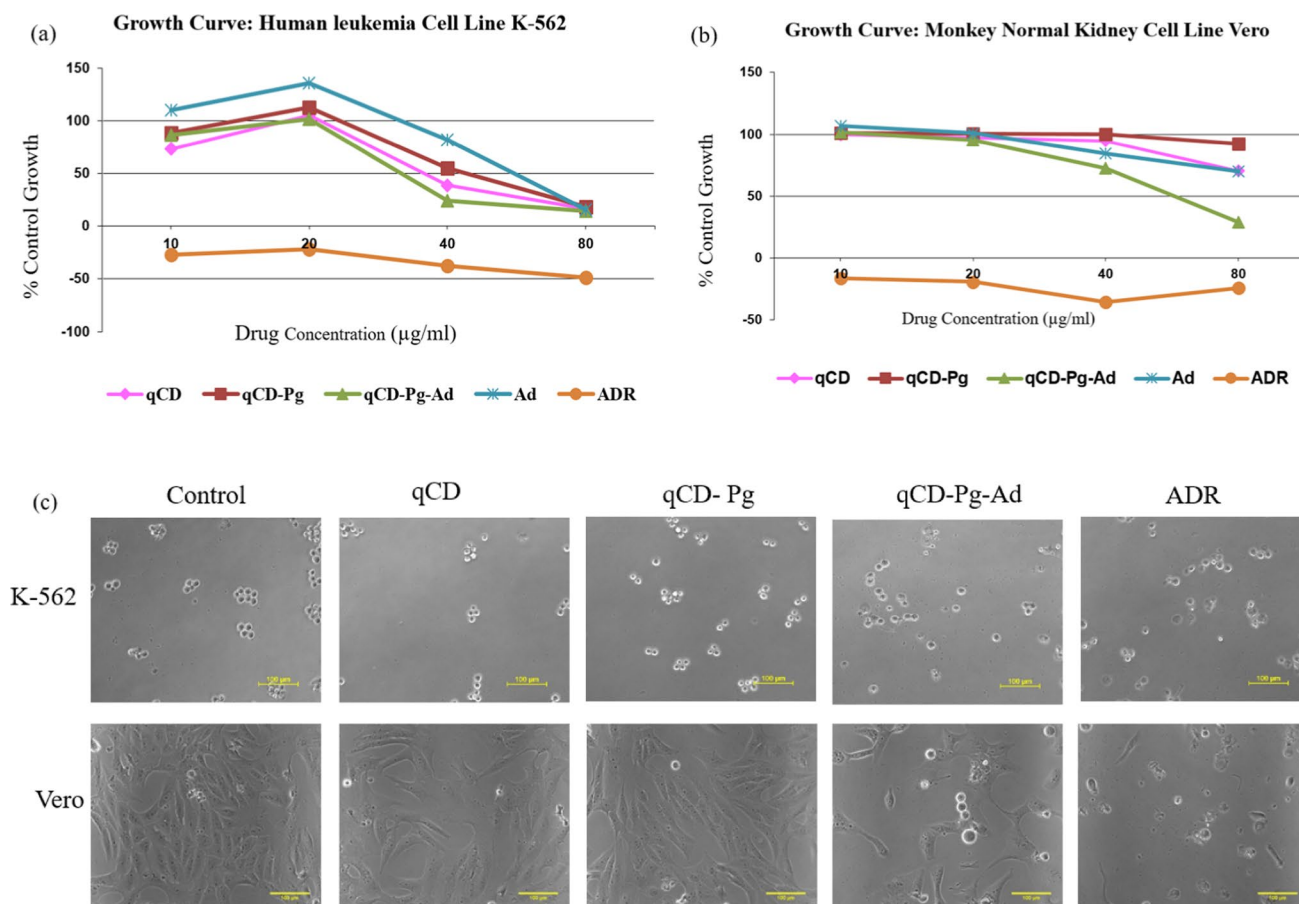| Spiked As^{3+} concentration (µM)	Theoretical concentration in final solution (µM)	Experimental concentration (µM)	Recovery (%)	% RSD
50	25	24.56 ± 0.213	98.24	0.867
Spiked Fe^{3+} concentration (µM)	Theoretical concentration in final solution (µM)	Experimental concentration (µM)	Recovery (%)	% RSD
50	25	24.87 ± 0.327	99.48	1.314

Results are represented as Mean $\pm$ SD, $n = 3$

Figure 6 SRB assay and brightfield photomicrographs of cells **a** Cytotoxic effect of CNDs on the % cell growth of K-562 leukemia cancer cell lines **b** Cytotoxic effect of CNDs on the % cell growth of normal vero cell lines and **c** Brighfield microscopy shows cell morphology of cells incubated with CNDs at 48 h.

Table 3 Zones of inhibition against different bacterial strains

Bacterial strain	Average radial diameter growth inhibition zone expressed in mean ± SEM (in mm)					
	qCD	qCD-Pg	qCD-Pg-Ad	Ad	Doxicyclin	DMSO
Enterobacter cloacae	12 ± 0.4	14 ± 0.5	15 ± 0.3*	12 ± 0.5	16 ± 0.9	–
Escherichia coli	7 ± 0.2	8 ± 0.8	16 ± 0.4*	7 ± 0.5	19 ± 0.7	–
Klebsiella pneumonia	–	–	–	–	16 ± 0.2	–
Staphylococcus aureus	–	–	–	–	21 ± 0.3	–
Enterococcus faecium	6 ± 0.8	8 ± 0.2	14 ± 0.4*	7 ± 0.6	15 ± 0.1	–

Results are represented as mean ± SD, *: significant at $p < 0.05$

was dropped onto paper disks. The doxicyclin (500 μg/mL) was used as a positive control, and DMSO was used as negative control. The results of the disk diffusion assay are shown in Table 3 and Figure S3. The doxycycline showed a clear zone of inhibition against all the screened MDR bacterial strains, reflecting the sensitivity of the used bacteria to the antimicrobial agent. The DMSO as negative control showed no zone of inhibition. Except *Klebsiella pneumonia* and *Staphylococcus aureus*, the qCD, qCD-Pg, qCD-Pg-Ad, and Ad showed the clear zone of inhibitions against the screened microbes (Figure S3). The qCD-Pg-Ad showed significantly more zone of inhibition compared to free Ad. Nanoparticles such as these carbon
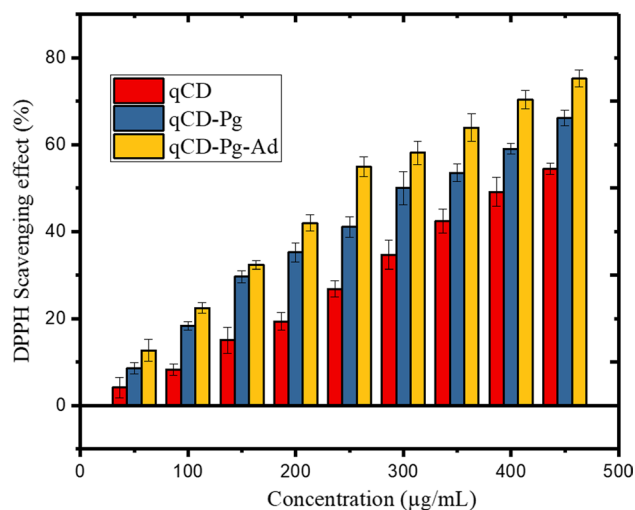
Figure 7 Percentage DPPH scavenging activity of qCD, qCD-Pg, and qCD-Pg-Ad at different concentrations.

nanodots can rupture the membrane and create free radicals, leading to their death [57, 58]. This is owing to their smaller size and the high surface-to-volume ratio of nanoparticles.

Free radical scavenging potential of CNDs

Dose-dependent free radicals scavenging potential of qCD, qCD-Pg, and qCD-Pg-Ad was observed from the DPPH assay (Fig. 7). DPPH was converted into a stable DPPH-H complex after accepting a hydrogen radical, which made the solution pale yellow from deep violet. The leftover DPPH was determined by comparing absorbance to blank at 515 nm. It can be inferred from the obtained results that the free radical scavenging potential of qCD was improved after surface passivation with PEG and subsequent conjugation with Ad.

Conclusion

Overall, this study reported quercetin-derived CNDs employing hydrothermal method and were further characterized by XPS, XRD, HRTEM, FTIR, TGA, and Zeta potential. The fabricated CNDs (as photomedicine) from quercetin (as phytomedicine) exhibited noteworthy characteristics such as a nanocarrier for the model drug andrographolide against leukemia cells, as a nanoprobe for sensing As^{3+} and Fe^{3+},

antibacterial potential against MDR bacteria, and free radical scavenging capability. Our findings revealed that quercetin-based carbon nanodots are good contenders for various healthcare applications.

Author contributions

GGN contributed to the study conception and design. Material preparation, data collection and analysis were performed by GGN, RP, DM and SS. The first draft of the manuscript was written by GGN, and all authors commented on previous versions of the manuscript. All authors read and approved the final manuscript. DKS, ASP, AP and ANS contributed to conceptualization, supervision, investigation, project administration, reviewing and editing functions.

Funding

Not applicable.

Declarations

Conflict of interest   The authors declare no conflict of interest.

References

[1] Marin R, Benayas A, García-Carillo N et al (2022) Nanoprobes for biomedical imaging with tunable near-infrared optical properties obtained via green synthesis. Adv Photon Res 3:2100260–2100270. https://doi.org/10.1002/adpr.202100260

[2] Su L, Qin S, Cai Y et al (2022) Co, N-doped carbon dot nanozymes with acid pH-independence and substrate selectivity for biosensing and bioimaging. Sens Actuators B: Chem 353:131150–131155. https://doi.org/10.1016/j.snb.2021.131150

[3] Naik GG, Minocha T, Verma A et al (2022) Asparagus racemosus root-derived carbon nanodots as a nano-probe for biomedical applications. J Mater Sci 57:20380–20401. https://doi.org/10.1007/s10853-022-07908-z

[4] Naik GG, Alam MB, Pandey V et al (2020) Pink fluorescent carbon dots derived from the phytomedicine for breast cancer cell imaging. ChemistrySelect 5(23):6954–6960

[5] Naik GG, Shah J, Balasubramaniam AK, Sahu AN (2021) Applications of natural product-derived carbon dots in cancer biology. Nanomedicine 16:587–608. https://doi.org/10.2217/nnm-2020-0424

[6] Wang B, Song H, Qu X et al (2021) Carbon dots as a new class of nanomedicines: opportunities and challenges. Coord Chem Rev 442:214010–214025. https://doi.org/10.1016/j.ccr.2021.214010

[7] Design and synthesis of dual-responsive carbon nanodots loaded with cisplatin for targeted therapy of lung cancer therapy and nursing care | SpringerLink. https://link.springer.com/article/https://doi.org/10.1007/s10876-020-01959-5. Accessed 27 Mar 2023

[8] John TS, Yadav PK, Kumar D et al (2020) Highly fluorescent carbon dots from wheat bran as a novel drug delivery system for bacterial inhibition. Luminescence 35:913–923. https://doi.org/10.1002/bio.3801

[9] Shen N, Wang T, Gan Q et al (2022) Plant flavonoids: classification, distribution, biosynthesis, and antioxidant activity. Food Chem 383:132531-132539. https://doi.org/10.1016/j.foodchem.2022.132531

[10] Huang C, Zhou Y, Yu G et al (2021) Glutathione-functionalized long-period fiber gratings sensor based on surface plasmon resonance for detection of As3+ ions. Nanotechnology. https://doi.org/10.1088/1361-6528/ac1b56

[11] Mohapatra D, Pratap R, Pandey V et al (2023) Bioengineered dual fluorescent carbon nano dots from Indian long pepper leaves for multifaceted environmental and health utilities. Environ Sci Pollut Res 30:52182–52208. https://doi.org/10.1007/s11356-023-25887-9

[12] Aa D, Shegokar R (2016) Polyethylene glycol (PEG): a versatile polymer for pharmaceutical applications. Expert Opin Drug Deliv 13;1257–1275 https://doi.org/10.1080/17425247.1182485

[13] Pharmacological effects and safety of Andrographis paniculata (Burm.f.) Nees - Tian - 2022 - Journal of Food Science - Wiley Online Library. https://ift.onlinelibrary.wiley.com/doi/full/https://doi.org/10.1111/1750-3841.16079. Accessed 27 Mar 2023

[14] Tj W (1990) Amplification and direct sequencing of fungal ribosomal RNA genes for phylogenetics. PCR protocols : a guide to methods and applications 315–322

[15] Shi N, Sun K, Zhang Z et al (2021) Amino-modified carbon dots as a functional platform for drug delivery: load-release mechanism and cytotoxicity. J Ind Eng Chem 101:372–378. https://doi.org/10.1016/j.jiec.2021.05.046

[16] Zhou C, Li H, Liu Y, Wang K (2022) Design and synthesis of dual-responsive carbon nanodots loaded with cisplatin for targeted therapy of lung cancer therapy and nursing care. J Clust Sci 33:331–338. https://doi.org/10.1007/s10876-020-01959-5

[17] Borman P, Elder D (2017) Q 2 (R1) Validation of Analytical Procedures: Text and Methodology, ICH quality guidelines: an implementation guide; 127–166

[18] Kholiya F, Chatterjee S, Bhojani G et al (2020) Seaweed polysaccharide derived bioaldehyde nanocomposite: potential application in anticancer therapeutics. Carbohydr Polym 240:116282–116291. https://doi.org/10.1016/j.carbpol.2020.116282

[19] Souri D, Salimi N, Ghabooli M (2021) Hydrothermal fabrication of pure ZnSe nanocrystals at different microwave irradiation times and their disc-diffusion antibacterial potential against Gram negative bacteria: bio-optical advantages. Inorg Chem Commun 123:108345–108349. https://doi.org/10.1016/j.inoche.2020.108345

[20] Davin-Regli A, Pagès J-M (2015) Enterobacter aerogenes and Enterobacter cloacae; versatile bacterial pathogens confronting antibiotic treatment. Front Microbiol 6:392–397

[21] Ramírez-Castillo FY, Moreno-Flores AC, Avelar-González FJ et al (2018) An evaluation of multidrug-resistant Escherichia coli isolates in urinary tract infections from Aguascalientes, Mexico: cross-sectional study. Ann Clin Microbiol Antimicrob 17:34. https://doi.org/10.1186/s12941-018-0286-5

[22] Bassetti M, Righi E, Carnelutti A et al (2018) Multidrug-resistant Klebsiella pneumoniae: challenges for treatment, prevention and infection control. Expert Rev Anti Infect Ther 16:749–761. https://doi.org/10.1080/14787210.2018.1522249

[23] Grady R, Hayes F (2003) Axe-Txe, a broad-spectrum proteic toxin-antitoxin system specified by a multidrug-resistant, clinical isolate of Enterococcus faecium. Mol Microbiol 47:1419–1432. https://doi.org/10.1046/j.1365-2958.2003.03387.x

[24] Hiramatsu K, Katayama Y, Matsuo M et al (2014) Multi-drug-resistant Staphylococcus aureus and future chemotherapy. J Infect Chemother 20:593–601. https://doi.org/10.1016/j.jiac.2014.08.001

[25] Alamu EO, Maziya-Dixon B, Menkir A, et al (2021) Bioactive composition and free radical scavenging activity of fresh orange maize hybrids: impacts of genotype, maturity stages, and processing methods. Front Nutr 8:640563–640568.

[26] Rajani M, Shrivastava N, Ravishankara MN (2000) A rapid method for isolation of andrographolide from Andrographis Paniculata Nees (Kalmegh). Pharm Biol 38:204–209. https://doi.org/10.1076/1388-0209(200007)3831-SFT204

[27] Hailing Y, Xiufang L, Lili W et al (2020) Doxorubicin-loaded fluorescent carbon dots with PEI passivation as a drug delivery system for cancer therapy. Nanoscale 12:17222–17237. https://doi.org/10.1039/D0NR01236J

[28] Kong T, Hao L, Wei Y et al (2018) Doxorubicin conjugated carbon dots as a drug delivery system for human breast cancer therapy. Cell Prolif 51:e12488–e12494. https://doi.org/10.1111/cpr.12488

[29] Yuan Y, Guo B, Hao L et al (2017) Doxorubicin-loaded environmentally friendly carbon dots as a novel drug delivery system for nucleus targeted cancer therapy. Colloids Surf, B 159:349–359. https://doi.org/10.1016/j.colsurfb.2017.07.030

[30] Hu S, Yang W, Li N et al (2018) Carbon-dot-based heterojunction for engineering band-edge position and photocatalytic performance. Small 14:1803447–1803453. https://doi.org/10.1002/smll.201803447

[31] Zhang M, Ju H, Zhang L et al (2015) Engineering iodine-doped carbon dots as dual-modal probes for fluorescence and X-ray CT imaging. Int J Nanomed 10:6943–6953. https://doi.org/10.2147/IJN.S82778

[32] Nigam P, Waghmode S, Louis M et al (2014) Graphene quantum dots conjugated albumin nanoparticles for targeted drug delivery and imaging of pancreatic cancer. J Mater Chem B 2:3190–3195. https://doi.org/10.1039/C4TB00015C

[33] Shamsipour M, Mansouri AM, Moradipour P (2019) Temozolomide conjugated carbon quantum dots embedded in core/shell nanofibers prepared by coaxial electrospinning as an implantable delivery system for cell imaging and sustained drug release. AAPS PharmSciTech 20:259–272. https://doi.org/10.1208/s12249-019-1466-0

[34] Singh B, Singh S, Gautam A et al (2022) Preparation and characterization of PLA microspheres as drug delivery system for controlled release of Cetirizine with carbon dots as drug carrier. Polym Bull. https://doi.org/10.1007/s00289-022-04331-x

[35] Saneja A, Kumar R, Singh A et al (2017) Development and evaluation of long-circulating nanoparticles loaded with betulinic acid for improved anti-tumor efficacy. Int J Pharm 531:153–166. https://doi.org/10.1016/j.ijpharm.2017.08.076

[36] Saraswat V, Kumari R, Yadav M (2022) Novel carbon dots as efficient green corrosion inhibitor for mild steel in HCl solution: electrochemical, gravimetric and XPS studies. J Phys Chem Solids 160:110341–110349. https://doi.org/10.1016/j.jpcs.2021.110341

[37] Liu J, Kong T, Xiong H-M (2022) Mulberry-leaves-derived red-emissive carbon dots for feeding silkworms to produce brightly fluorescent silk. Adv Mater 34:e2200152–e2200157. https://doi.org/10.1002/adma.202200152

[38] Du J, Xu N, Fan J et al (2019) Carbon dots for in vivo bioimaging and theranostics. Small 15:e1805087–e1805099. https://doi.org/10.1002/smll.201805087

[39] Kailasa SK, Ha S, Baek SH et al (2019) Tuning of carbon dots emission color for sensing of Fe3+ ion and bioimaging applications. Mater Sci Eng C Mater Biol Appl 98:834–842. https://doi.org/10.1016/j.msec.2019.01.002

[40] Tian X, Chen L, Li Y et al (2017) Design and synthesis of a molecule with aggregation-induced emission effects and its application in the detection of arsenite in groundwater. J Mater Chem 5:3669–3672. https://doi.org/10.1039/C7TC00363C

[41] Highly Selective Turn-On Fluorogenic Chemosensor for Robust Quantification of Zn(II) Based on Aggregation Induced Emission Enhancement Feature | ACS Sensors. https://pubs.acs.org/doi/full/https://doi.org/10.1021/acssensors.6b00289?casa_token=5KQns-7-RRAAAAAA%3ApLQzrjEN5CMGcMs7mrspJghOxeum1qd19ak2VYejR_ntIr9QHGHHZ9pPDeTLZxpmsBxQtxDfHvxgV2M-dQ. Accessed 27 Mar 2023

[42] Chen J, Law CCW, Lam JWY et al (2003) Synthesis, light emission, nanoaggregation, and restricted intramolecular rotation of 1,1-Substituted 2,3,4,5-Tetraphenylsiloles. Chem Mater 15:1535–1546. https://doi.org/10.1021/cm021715z

[43] Kumar ASK, Jiang S-J (2017) Synthesis of magnetically separable and recyclable magnetic nanoparticles decorated with β-cyclodextrin functionalized graphene oxide an excellent adsorption of As(V)/(III). J Mol Liq 237:387–401. https://doi.org/10.1016/j.molliq.2017.04.093

[44] Gurung S, Neha, Arun N, et al (2023) Dual metal ion (Fe3+ and As3+) sensing and cell bioimaging using fluorescent carbon quantum dots synthesised from Cynodon dactylon. Chemosphere 339:139638–139646. https://doi.org/10.1016/j.chemosphere.2023.139638

[45] Bayazeed Alam M, Hassan N, Sahoo K et al (2022) Deciphering interaction between chlorophyll functionalized carbon quantum dots with arsenic and mercury toxic metals in water as highly sensitive dual-probe sensor. J Photochem Photobiol A: Chem 431:114059–114071. https://doi.org/10.1016/j.jphotochem.2022.114059

[46] Zhao X, Liao S, Wang L et al (2019) Facile green and one-pot synthesis of purple perilla derived carbon quantum dot as a fluorescent sensor for silver ion. Talanta 201:1–8. https://doi.org/10.1016/j.talanta.2019.03.095

[47] Qi H, Teng M, Liu M et al (2019) Biomass-derived nitrogen-doped carbon quantum dots: highly selective fluorescent probe for detecting Fe3+ ions and tetracyclines. J Colloid Interface Sci 539:332–341. https://doi.org/10.1016/j.jcis.2018.12.047

[48] Khan ZMSH, Rahman RS, Shumaila et al (2019) Hydrothermal treatment of red lentils for the synthesis of fluorescent carbon quantum dots and its application for sensing Fe3+. Optic Mater 91:386–395. https://doi.org/10.1016/j.optmat.2019.03.054

[49] Wang J, Sheng Li R, Zhi Zhang H et al (2017) Highly fluorescent carbon dots as selective and visual probes for sensing copper ions in living cells via an electron transfer process. Biosens Bioelectron 97:157–163. https://doi.org/10.1016/j.bios.2017.05.035

[50] Liu R, Gao M, Zhang J et al (2015) An ionic liquid promoted microwave-hydrothermal route towards highly photoluminescent carbon dots for sensitive and selective detection of iron(III). RSC Adv 5:24205–24209. https://doi.org/10.1039/C5RA00089K

[51] Zhu S, Meng Q, Wang L et al (2013) Highly photoluminescent carbon dots for multicolor patterning, sensors, and bioimaging. Angew Chem Int Ed 52:3953–3957. https://doi.org/10.1002/anie.201300519

[52] Cancer statistics, 2023 - Siegel - 2023 - CA: A Cancer Journal for Clinicians - Wiley Online Library. https://acs-journals.onlinelibrary.wiley.com/doi/https://doi.org/10.3322/caac.21763. Accessed 25 Mar 2023

[53] Liao H-C, Chou Y-J, Lin C-C et al (2019) Andrographolide and its potent derivative exhibit anticancer effects against imatinib-resistant chronic myeloid leukemia cells by down-regulating the Bcr-Abl oncoprotein. Biochem Pharmacol 163:308–320. https://doi.org/10.1016/j.bcp.2019.02.028

[54] Yang T, Yao S, Zhang X, Guo Y (2016) Andrographolide inhibits growth of human T-cell acute lymphoblastic leukemia Jurkat cells by downregulation of PI3K/AKT and upregulation of p38 MAPK pathways. Drug Des Devel Ther 10:1389–1397. https://doi.org/10.2147/DDDT.S94983

[55] Zhao D, Li X, Xu M et al (2023) Preparations of anti-bacterial yellow-green-fluorescent carbon dots and carbon dots-lysozyme complex and their applications in bacterial imaging and bacteria/biofilm inhibition/clearance. Int J Biol Macromol 231:123303–123311. https://doi.org/10.1016/j.ijbiomac.2023.123303

[56] Zhao D, Xu M, Dai K et al (2023) The preparation of chiral carbon dots and the study on their antibacterial abilities. Mater Chem Phys 295:127144. https://doi.org/10.1016/j.matchemphys.2022.127144

[57] Hajipour MJ, Fromm KM, Akbar Ashkarran A et al (2012) Antibacterial properties of nanoparticles. Trends Biotechnol 30:499–511. https://doi.org/10.1016/j.tibtech.2012.06.004

[58] Naik GG, Alam MB, Pandey V, Mohapatra D et al (2020) Multi-functional carbon dots from an ayurvedic medicinal plant for cancer cell bioimaging applications. J Fluoresc 30:407–418